Radio Interferometer Observations and Analysis of an Energetic In-Cloud Pulse Based on Ensemble Empirical Mode Decomposition

Xiangpeng Fan, Paul R. Krehbiel, Julia N. Tilles, Mark A. Stanley, Seda Senay, Harald E. Edens, William Rison, and Yijun Zhang

***Abstract*— Based on the ensemble empirical mode decomposition (EEMD) method, a DAF method for signal construction is proposed that repeatedly decomposes (D) the signal, amplifies (A) the local signal characteristics, and then filters (F) the signal. This method is used to decompose and reconstruct the electric field waveform (called a sferic) of an energetic in-cloud pulse (EIP) with a 247-kA peak current detected by a fast antenna (FA). Based on synchronous sub-microsecond very high-frequency (VHF, 14–88 MHz) radio interferometer (INTF) observations and observed downward fast positive and upward fast negative breakdowns, which occurred simultaneously with the EIP, the EIP sferic is decomposed by the DAF method in 11 steps into two independent sferics: a smoother filtered EIP sferic and an embedded narrow bipolar-like event (NBE). It is verified that strong VHF radiation is generated by the NBE-like event, rather than being associated with the smooth EIP sferic. The analysis, decomposition, and reconstruction of the correlated signals by the EEMD-based DAF method proposed in this article support the idea that the large-amplitude EIP sferic was generated by relativistic discharge responsible for an accompanying terrestrial gamma-ray flash (TGF) rather than by streamer or leader activity.**

***Index Terms*— Energetic in-cloud pulse (EIP), ensemble empirical mode decomposition (EEMD), lightning signal analysis, terrestrial gamma-ray flash (TGF).**

Manuscript received October 16, 2020; revised April 11, 2021; accepted May 4, 2021. This work was supported in part by National Science Foundation under Grant AGS 1720600, in part by the National Natural Science Foundation of China under Grant 41875001, and in part by China Postdoctoral Science Foundation under Grant 2020M670974. *(Corresponding author: Xiangpeng Fan.)*

Xiangpeng Fan is with the Department of Atmospheric and Oceanic Sciences, Fudan University, Shanghai 200438, China, also with the Institute of Atmospheric Sciences, Fudan University, Shanghai 200438, China, and also with the State Key Laboratory of Severe Weather (LASW), Chinese Academy of Meteorological Sciences, Beijing 100081, China (e-mail: fanxp@cma.gov.cn).

Paul R. Krehbiel, Mark A. Stanley, Harald E. Edens, and William Rison are with the Langmuir Laboratory for Atmospheric Research, Geophysical Research Center, New Mexico Institute of Mining and Technology, Socorro, NM 87801 USA (e-mail: krehbiel@ibis.nmt.edu; sparky@mark-stanley.name; harald.edens@nmt.edu; rison.bill@gmail.com).

Julia N. Tilles is with the Electrical Sciences and Experiments Division, Sandia National Laboratories, Albuquerque, NM 87123 USA (e-mail: jntille@sandia.gov).

Seda Senay is with the Electrical Engineering Department, New Mexico Institute of Mining and Technology, Socorro, NM 87801 USA (e-mail: seda.senay@nmt.edu).

Yijun Zhang is with the Department of Atmospheric and Oceanic Sciences, Fudan University, Shanghai 200438, China (e-mail: zhangyijun@fudan.edu.cn).

Digital Object Identifier 10.1109/TGRS.2021.3078738

I. Introduction

A TERRESTRIAL gamma-ray flash (TGF) is a burst of energetic (up to tens of mega electron volts) photons produced in the Earth's atmosphere that was first discovered by the Burst and Transient Source Experiment onboard the Compton Gamma Ray Observatory [1]. TGFs, which are the result of bremsstrahlung by relativistic runaway electrons, have durations spanning less than 1 ms [2], [3]. Preliminary measurements of low-frequency (LF) electric field waveforms (160 Hz–500 kHz) indicate that TGFs are generated during intracloud (IC) lightning [4]. Through the analysis of LF electromagnetic fields [5]–[7] waveforms (often called "sferics"), as well as very high-frequency (VHF) lightning mapping detection systems [8]–[10], researchers have found that TGFs occur when normal polarity [11] lightning develops upward. Other observational studies have shown that the electromagnetic pulse amplitude of a sferic matches the temporal variation of the photon intensity of a TGF [6], [12], [13], indicating that sferics are produced by TGF-generating discharge processes [12], [13].

In recent years, a special kind of cloud flash radio electric field pulse with a high peak current called an energetic in-cloud pulse (EIP) has attracted the attention of researchers, and these EIPs were discovered to coincide with TGFs [14], [15]. Based on further research, a one-to-one correspondence was discovered between EIPs and TGFs that occur within the range of a spacecraft detector [16], [17], so that EIPs can serve as proxies for a subpopulation of TGFs, and observed EIP sferics have been noted to develop independently of the VHF emissions generally associated with streamer activity [19]–[22]. To understand how EIPs are generated and to better understand the TGF generation mechanism, Tilles *et al.* [18] recently conducted in-depth research and analysis on an EIP through synchronous observations from multiple detection devices in different frequency bands. Sub-microsecond VHF radio mapping of the EIP provided an order of magnitude finer time resolution than previously reported TGF-related VHF observations [8]–[10], [16]. Furthermore, Tilles *et al.* [18] provided strong evidence that the EIP sferic was not produced by conventional lightning processes (i.e., streamers and leaders).

In this work, we describe the advanced technique that was used to separate the sferic waveforms into their two

components, namely, to separate the smooth part corresponding to the relativistic discharge of the EIP from the embedded streamer activity of a narrow bipolar-like event (NBE) that was triggered by the relativistic discharge. By applying ensemble empirical mode decomposition (EEMD) [23] in an advanced and highly innovative manner, we were able to separate two overlapping events. Accordingly, the NBE-like part of the waveform was shown more correctly, both qualitatively and quantitatively. In addition to separating out the waveform components, this analysis allowed the NBE-like event to be quantitatively evaluated.

II. Instrumentation and Observations

On September 24, 2016, strong cloud lightning occurred near the Kennedy Space Center (KSC) on the East Florida coast. The peak current of the lightning detected by the National Lightning Detection Network (NLDN) was 247.3 kA. This high-current discharge event was subsequently identified as an EIP by the LF magnetic field sensor [12] of Duke University, Durham, NC, USA, which was deployed at the Florida Institute of Technology, Melbourne, FL, USA. The 3-D VHF lightning mapping array (LMA) at Kennedy Space Center (KSC-LMA) [24], [25] also observed the EIP lightning. In addition, both the broadband VHF interferometer (INTF) and fast antenna (FA) [19], [26], which also deployed by New Mexico Tech (NMT), Socorro, NM, USA, and operated at KSC in 2016–2017, detected this EIP lightning case.

A. Instrumentation

The LMA can provide 3-D location information of lightning radiation sources. Seven LMA stations were located within the boundaries of KSC and Cape Canaveral Air Force Station; in order to provide LMA with greater coverage of thunderstorms and lightning, three outlying stations were deployed 60–100-km inland, extending southward along the Florida coast. The LMA network uses 60–66-MHz bandpass signals to locate impulsive events above the threshold value in successive 80-μs time windows by measuring the arrival time difference. The temporal accuracy of the location system reaches 25–30-ns rms. In the analysis of the physical mechanisms, developmental characteristics, etc. of the EIP, in addition to determining the overall structure and development of the parent lightning, the LMA observations also estimate the position of the EIP in 3-D, and provide very important background information about the developmental characteristics and charge structure of the parent storm.

The analyses are not dependent on the range of the lightning flash from the INTF. Rather, they depend only on the superimposed activity being detectable. Due to their ability of EMD techniques, in general, to distinguish between signals having different physical characteristics from each other, and the noise reduction abilities of EMD, even weak signals can be extracted from superimposed activity. In the present case, the parent lightning flash was sufficiently close (30 km) for its activity to be readily detected by the INTF and FA. In addition, the NBE-like signal was reasonably noticeable on the EIP sferic, allowing its waveform to be readily distinguished.

For parent lightning and EIP, more accurate positioning results are given by INTF. As the examples given in previous studies [19], INTF has unique advantages in the analysis of small-scale physical processes of tens of microseconds. It uses three broadband VHF (14–88 MHz) flat receiving antennas on a 100-m baseline arranged in equilateral triangles to determine the 2-D direction of arrival of VHF radiation events with sub-microsecond time resolution. The time-series waveforms for each receiver of INTF and FA were recorded simultaneously on four channels at a sampling rate of 180 MS/s and 16-bit resolution. This high temporal and sampling accuracy provide a strong guarantee for the fine analysis of discharge events. After processing the original waveforms, the locating algorithm acquires a VHF source with a window width of 1.4 μs (256 sampling points), with the adjacent windows advancing in steps of 0.35 μs (64 samples), thus generating a continuous, high-speed (0.35 μs), 2-D evolution image of the lightning discharge event.

In addition, the FA was sensitive from 3 kHz to $>$20 MHz, with a decay time constant of 100 μs. The ability to characterize the electric field changes of lightning discharge events with high sensitivity is an important aid to the analysis of lightning physical processes.

The combination of LMA, INTF, and FA observations provided detailed information on the altitude, physical range, propagation speed, and polarity of the EIP-related breakdown.

B. Observation of the EIP

According to the standard established by Lyu *et al.* [15], the sferic in Fig. 1(a) is characterized as an EIP due to its long pulsewidth (54 μs), its peak ratio being less than unity ($<$0.9), indicating that the amplitude of the secondary peak is higher than that of the initial peak, and its very low isolation ratio (18 dB), that is, the logarithmic ratio of the sum of sferic amplitudes before and during the event of interest.

Tilles *et al.* [18] analyzed the observational characteristics of the EIP, the development characteristics of the parent lightning, and the charge structure characteristics of thunderstorms during the occurrence of the EIP by using a variety of synchronous observation data and then discussed the physical mechanism responsible for the EIP event. Given that the focus of this article is to present the method and procedure for signal analysis of EIP sferic, only the results of the analysis of EIP given by Tilles *et al.* [18] are briefly presented here, which are as follows.

1) The EIP flash was initiated by an NBE event with relatively high power (46.6 dBW).
2) The negative leader propagated about 1.53 ms vertically upward at a relatively fast speed ($5 \times 10^5 - 3 \times 10^6$ m/s) compared to the typical in-cloud negative leader development ($1 - 3 \times 105$ m/s [27]–[29]).
3) Relatively fast negative breakdown (FNB) of 6×10^6 m/s started approximately 200 μs before the EIP and propagated vertically upward for more than 1 km with increasing VHF power.
4) The EIP is immediately preceded by a series of rapid ($10^7 - 10^8$ m/s) breakdown sequences of 10–20 μs

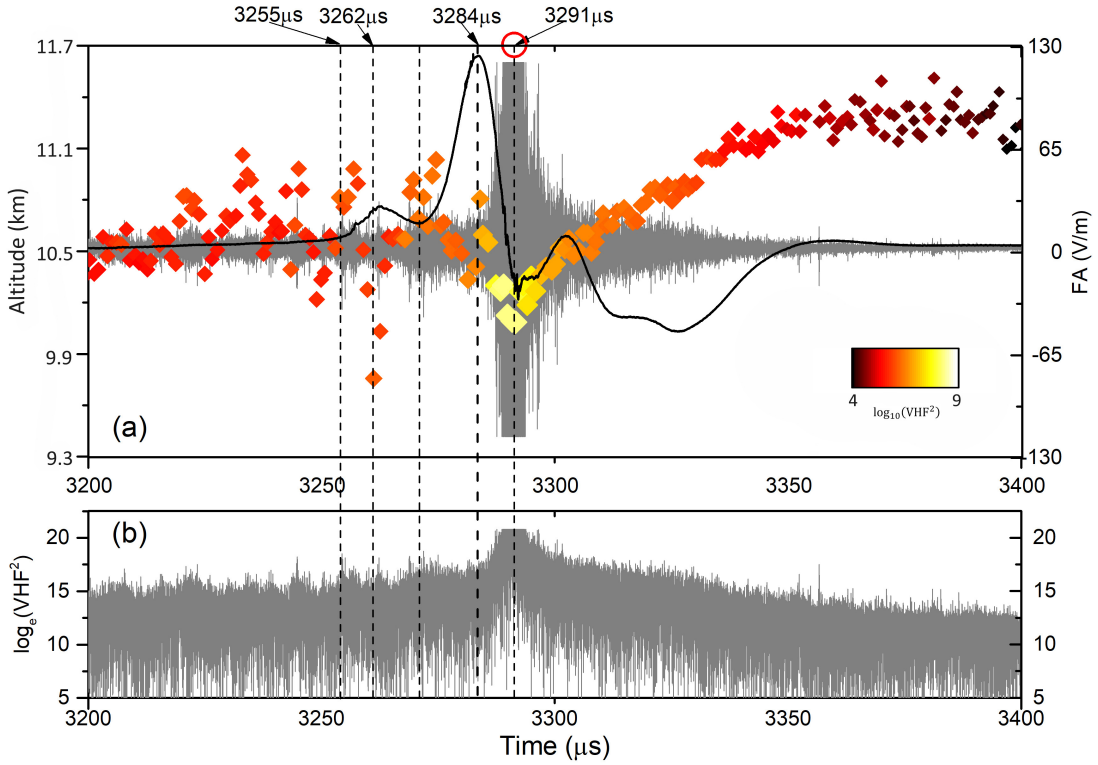

Fig. 1. Detailed evolution process of the EIP. (a) INTF sources during the EIP are shown in the altitude versus time plots (the altitude is calculated by matching the 3-D information obtained from LMA), colored, and resized according to the detected VHF power [log10(VHF2)]. (b) Natural logarithm of the VHF power shows that it starts to increase exponentially before the signal is saturated (dashed line at 3284 μs). More detailed evolution can be seen in [17].

duration and alternating downward/upward progression, and their oscillation amplitudes are expanding in the spatial range preceding the EIP.

5) The EIP occurred about 3 ms after lightning initiated, its duration was about 60 μs, and its peak current was given by NLDN as 247 kA. The EIP consisted of three sferic pulses caused by a relativistic discharge. During the large EIP sferic, the VHF radiation, which is generally associated with streamer activity [19]–[22], was very weak.
6) Shortly after the EIP sferic peak, a high-power (50.6 dBW) NBE-like event occurred. Similar to previous observations of NBEs [19], [30], this NBE-like event consisted of a downward fast positive breakdown (FPB) followed immediately by an upward FNB. These main features can be seen in the superposition of multiple observations in Fig. 1.

The EIP sferic in Fig. 1(a) illustrates that some micropulse events are superimposed on the relatively smooth curve of the EIP sferic near 3291 μs, and thus, it is intuitively impossible to confirm the similarities between these micropulse events and the typical electric field waveforms of NBEs. In the analysis of Tilles *et al.* [18], the NBE-like event and EIP sferics were separated by EEMD with a double-sided bidirectional mirror (DBM) extension method [23]. The separated NBE-like sferic was aligned in time with a distinct pulse in VHF radiation, as well as FPB and FNB located by the INTF. After separating the NBE-like sferic from the original EIP sferic, the filtered EIP sferic becomes smoother. These factors played important roles in confirming that the EIP was generated by relative feedback discharge rather than conventional lighting processes (i.e., streamers and leaders). We tried many of the commonly used analysis methods (Fig. 2 shows the results of envelope analysis) but failed to separate overlapping events until EEMD was applied in an advanced and highly innovative way. Here we introduce EEMD and its specific principles, steps, and analysis process to the decomposition and reconstruction of EIP sferics.

III. DBM_EEMD

A. EMD

Fan *et al.* [31] introduced the EMD algorithm to the analysis of lightning LF/very low-frequency (VLF) electric field signals to optimize the signal and improve the lightning location ability of lightning LF E-field detection arrays (LFEDAs). As an empirical and algorithm-defined method, EMD, which was first proposed by Huang *et al.* [32], it can adaptively decompose a complex signal into a set of intrinsic mode functions (IMFs). EMD can decompose a signal without setting the basis function in advance, and the degree of decomposition is adaptively determined according to the nature of the signal to be decomposed. The Hilbert transform is used to analyze the IMF components decomposed by EMD, and the fast Fourier transform (FFT) is used to obtain the unilateral spectrum characteristics of each IMF component; together, this approach is called the Hilbert–Huang transform (HHT). In recent years,

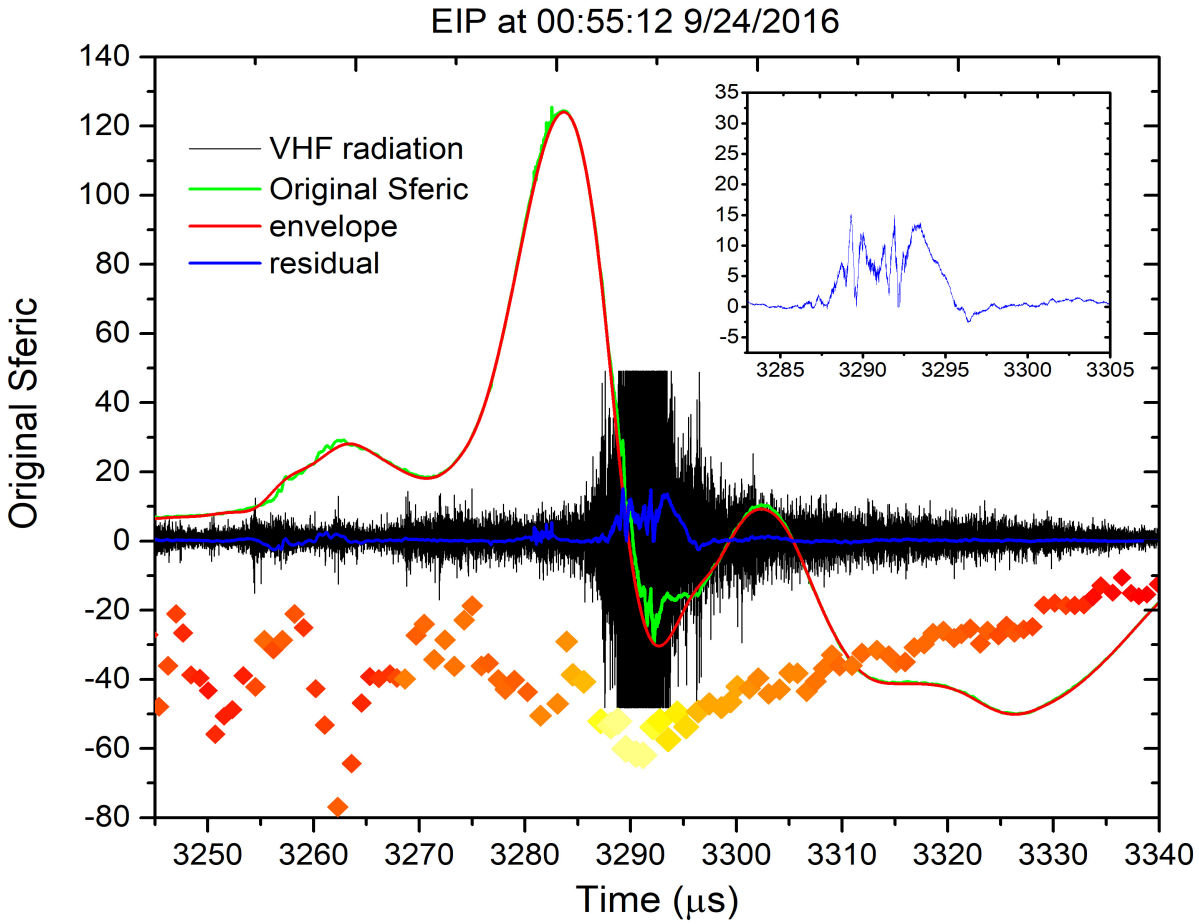

Fig. 2. Decomposition of the EIP sferic obtained by using envelope analysis. The green waveform is the original sferic, which was decomposed into two components. The red waveform is the lower envelope of the peak sferic. The blue one is the difference between the original sferic and the lower envelope, which can only be defined as a residual, as it clearly does not have the typical characteristics of an NBE sferic.

the excellent performance of the HHT in signal analysis, filtering, and noise reduction has been widely recognized, and the HHT has been adopted in many disciplines [33].

The EMD has unique advantages in the analysis of lightning electromagnetic field signals [31], [34]. However, the inherent mode mixing and endpoint effect of EMD can cause problems in the analysis of LF/VLF electric field change signals. Mode mixing is defined as a single IMF containing oscillations on significantly different scales or signals of similar scales that are decomposed into different IMF components caused by the discontinuity characteristics of signals [35]. As discussed by Huang *et al.* [32], discontinuities not only cause serious mode mixing in both the time and the frequency domains but also render the physical meaning of a single IMF unclear. Furthermore, mode mixing leads to the loss of pulse power and the retention of noise, and the endpoint effect leads to the distortion of the reconstructed signal.

B. EEMD

To overcome the inherent mode mixing of EMD, Wu and Huang [35] proposed a new technique known as EEMD, a highly effective noise-aided data analysis method. As shown in the flowchart of Fig. 3(a), EEMD adds white noise $n_i(t)$ to the original signal $x(t)$. Due to the uniform spectral distribution of white noise, the noise is automatically distributed to the appropriate reference scale. Because noise is characterized by a zero mean, the noise will be eliminated after several rounds of averaging calculations, so the ensemble mean can be directly regarded as the result. In contrast, the EEMD method with noise as an auxiliary analysis can decompose the main features of a simulated signal into different IMF components. From the simulation analysis of Fan *et al.* [23], the noise in each IMF component can be well suppressed.

In addition, due to the lack of extrema at the ends of signals, a large error will occur at the end of a signal in the process of fitting the upper and lower envelopes by using spline interpolation. This error further deteriorates the decomposition of the intermediate signal during the EMD sifting process, resulting in the pollution of the entire signal sequence; this is known as the endpoint effect of the EMD algorithm [33]. The existence of the endpoint effect will lead to signal distortion and consequently large errors in signal analysis using the resulting IMF components [23]. Many methods are available to suppress the endpoint effect.

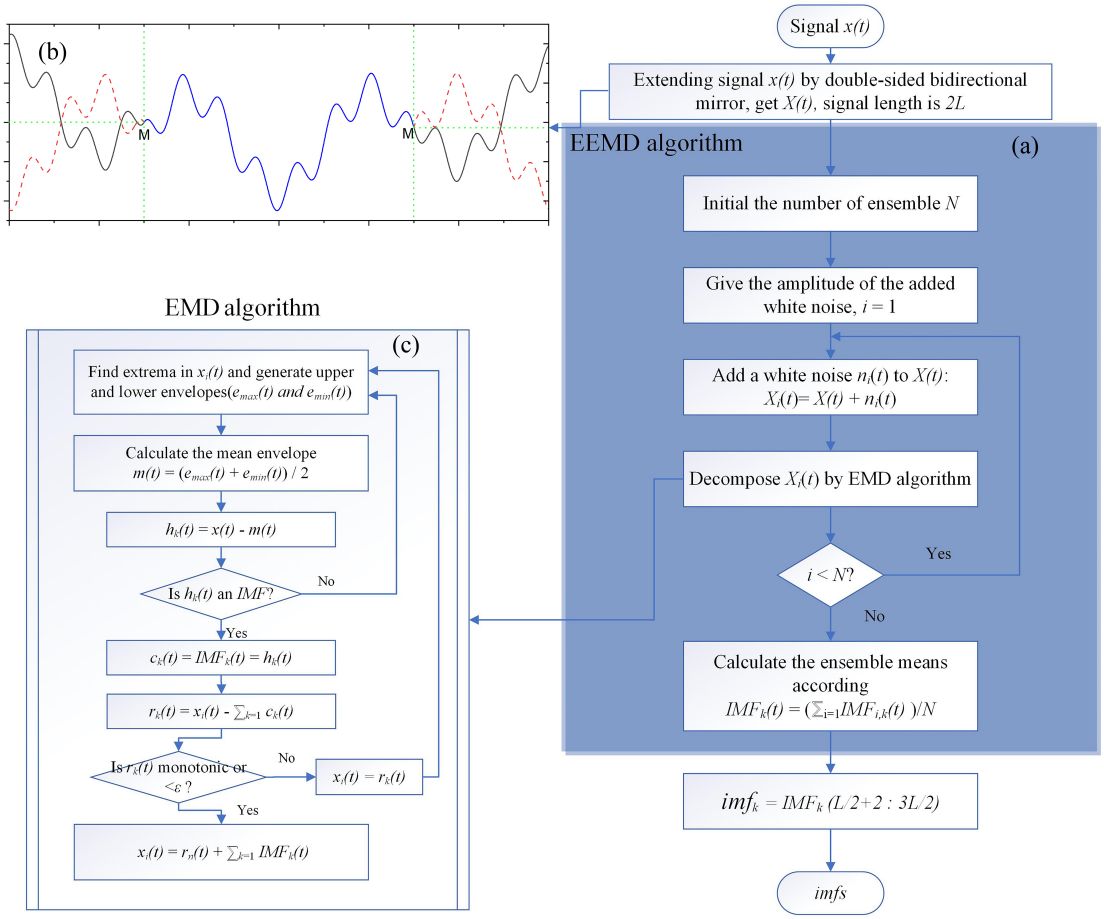

Fig. 3. Flowchart of the DBM_EEMD algorithm. (a) Flowchart of the EEMD algorithm. (b) DBM extension method. (c) Flowchart of the EMD algorithm.

In practical engineering applications, the mirror extension method [36] is more widely used because of its simplicity and versatility.

However, there are some limitations when employing the mirror extension method for signal analysis. In particular, as long as there is even a slight fluctuation at the end of the signal, regardless of whether it is of relatively HF or LF, the mirror extension signal and the original signal will merge to form a mutated signal, which is not differentiable at the mirror [23]. This nondifferentiable point can have a significant impact on the decomposition results and thus severely affect the positioning capability of the LF/VLF lightning positioning system. To solve the problems above, Fan *et al.* [23] proposed the DBM extension method. As shown in Fig. 3(b), compared with the general mirror extension method, the DBM method extends two mirror signals with half the length of the original signal from the left and right ends of the original signal [as shown by the red dotted line in Fig. 3(b)]. These two image signals are then reversed in the vertical direction to obtain a vertical image of each horizontal signal [as shown by the black solid line in Fig. 3(b)]. Hence, this mirror extension method is both double-sided (left and right) and bidirectional (horizontal and vertical). Finally, the extended image signal [black solid line in Fig. 3(b)] and the original signal are taken as the signal to be decomposed. DBM extension can effectively solve the signal mutation problem at the end of the original signal caused by mirror extension.

C. Decomposition and HHT Analysis of the EIP Sferic

As shown in Fig. 4, ten IMF components are obtained from the decomposition of the EIP sferic by DBM_EEMD. These IMF components reflect the local characteristics of the decomposed signal in the frequency and time domains [32]. Accordingly, the spectral distribution characteristics of each IMF component are acquired by the HHT, as shown in Fig. 5(a)–(c). Tilles *et al.* [18] determined that the physical EIP process started at 3255 μs. Combined with the decomposition results in Fig. 4 and the spectrum analysis in Fig. 5, the EIP sferic exhibits obvious frequency band distribution characteristics. The main components of IMFs 8–10 are located at VLF (3–30 kHz) and LF (30–300 kHz); the main components of IMFs 5–7 are located at a moderate frequency (300 kHz–3 MHz), and IMFs 1–4 contain weak HF (3–30 MHz) and even VHF (30–300 MHz) signals. Since there is a significant bandgap between the three IMF components in Fig. 5(b) and those in Fig. 5(c), we combine and reconstruct them separately. Furthermore, since the four IMF components in

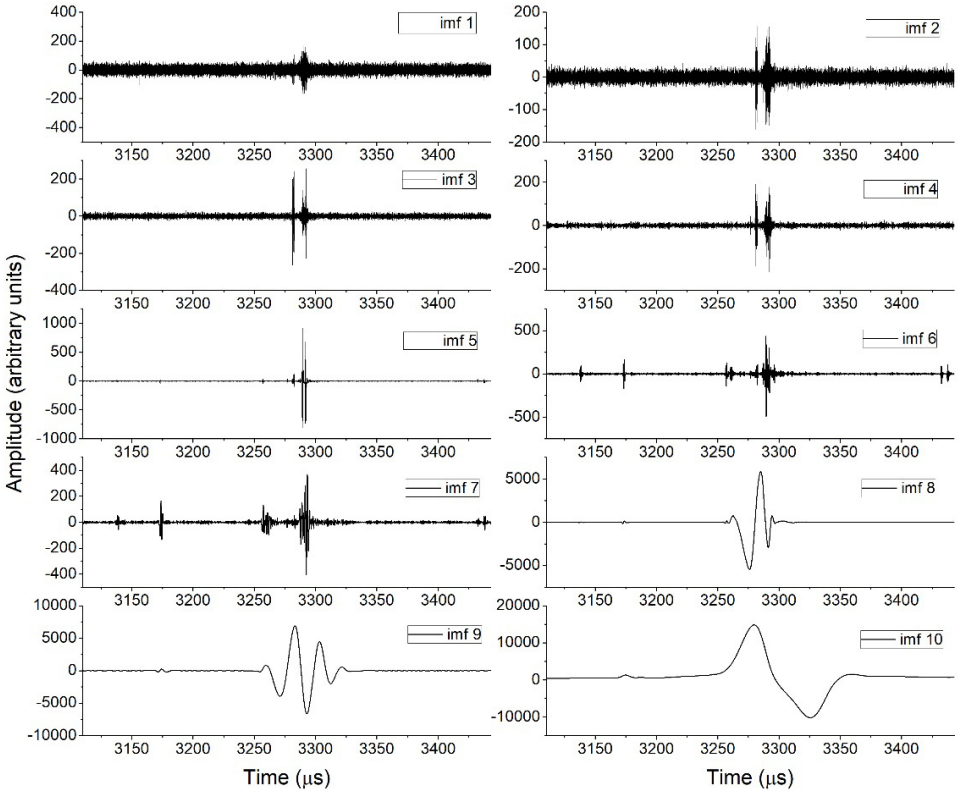

Fig. 4. EIP sferic decomposed by DBM_EEMD into ten IMF components with frequencies from high to low.

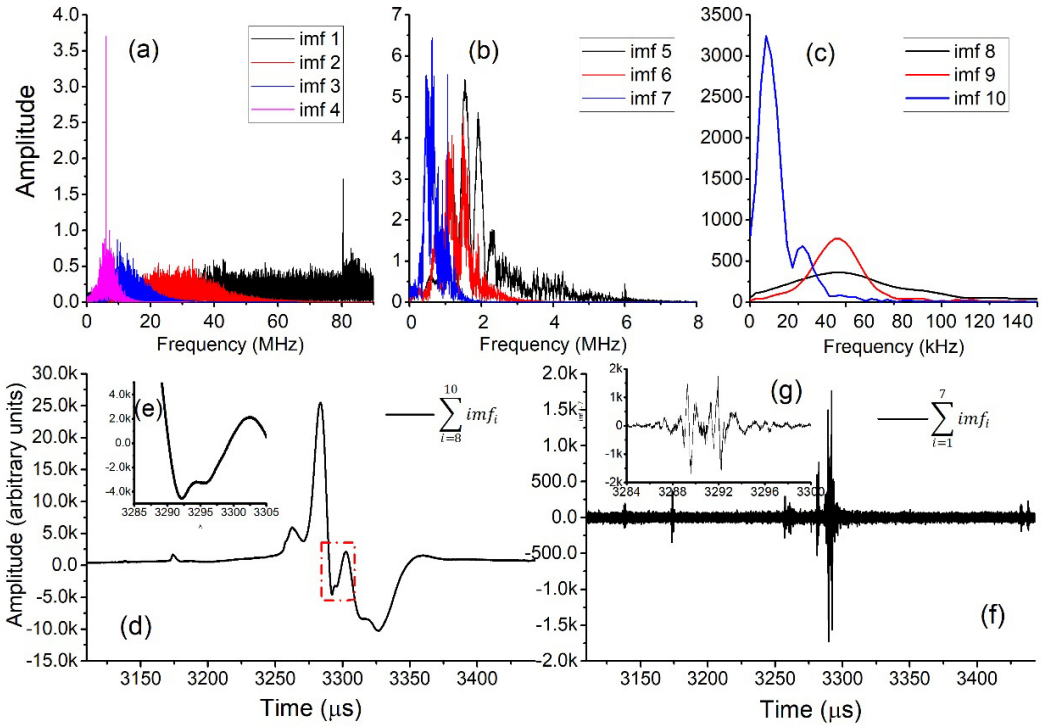

Fig. 5. Spectrum of the EIP sferic analyzed by the HHT, and reconstructed sferic decomposed into two individual signals. (a)–(c) Frequency distribution and amplitudes of different IMF components. (d) Reconstructed waveform containing IMFs 8–10. (e) Magnified view of the main area of concern in (d). (f) Reconstructed waveform containing IMFs 1–7. (g) Magnified view of the main area of concern in (f).

Fig. 5(a) have higher frequencies and weaker amplitudes and they are more closely related to the three IMF components in Fig. 5(b) in the time domain, we superimpose them with the three IMF components in Fig. 5(b). Thus, the EIP sferic is decomposed into two individual signals with significant differences, as shown in Fig. 5(d) and (f).

As shown in Fig. 1, the VHF radiation and LMA detection (red circle) near 3291 μs align in time with the onset of FNB

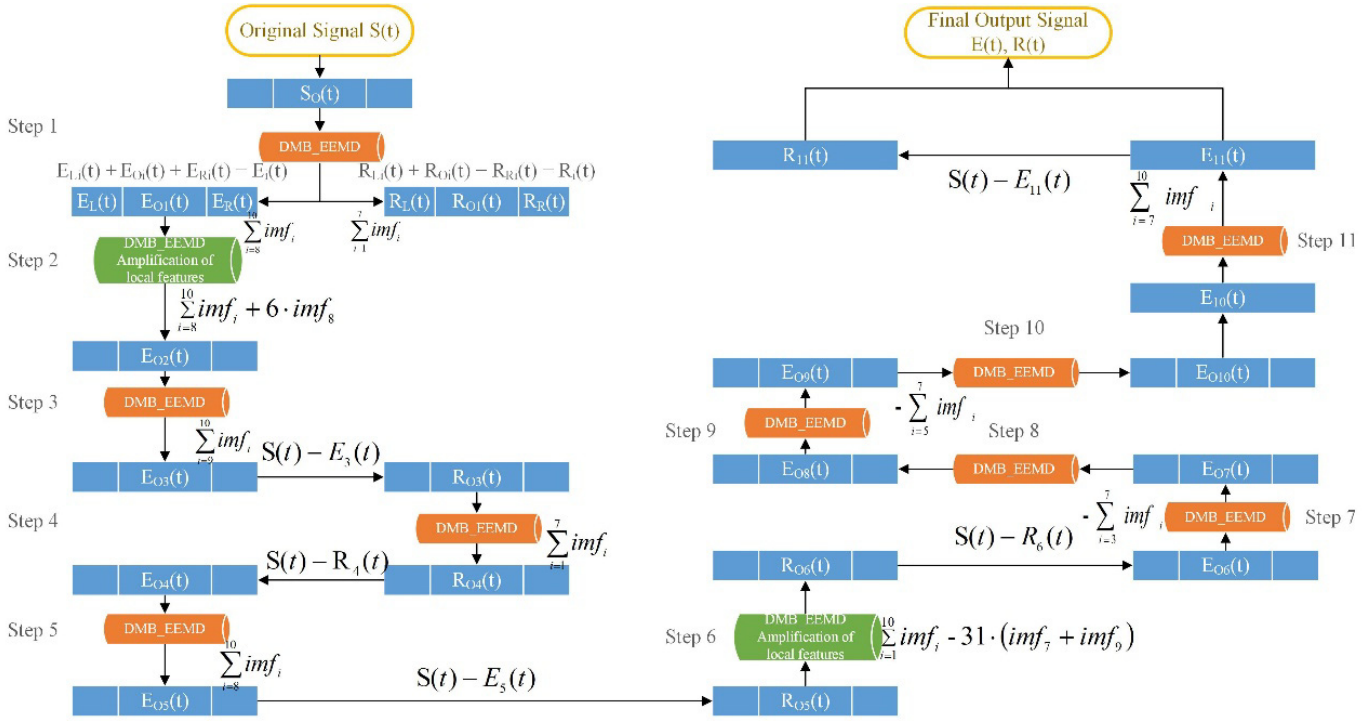

Fig. 6. Flowchart of separating the NBE-like sferic from the EIP sferic. DBM_EEMD is used to decompose (D) the local original sferic step by step, amplify (A) local features, and smooth and filter (F) the signal. In the flowchart, S denotes the original sferic, E represents the EIP component with the main LF components after reconstructing the IMFs [similar to the waveform in Fig. 5(d)], R represents the residual part of the signal ($R = S - E$), the corner marker O is the target signal to be decomposed, the corner marker L is the left part outside the target signal, and R is the right part outside the target signal. Taking signal E as an example, $E = E_L + E_O + E_R$.

as determined by the INTF. There is a 7-μs delay of the VHF radiation peak after the EIP sferic peak. However, on the sferic, there are significant subpulses near 3291 μs. These features help us to determine the physical mechanisms involved during the EIP and are the focus of this investigation.

The two sferic components near 3291 μs are locally magnified in Fig. 5(e) and (g). After the signals in different frequency bands are separated, a "platform" is detected near 3295 μs on the EIP sferic [indicated by the arrow in Fig. 5(e)], which makes the local frequency of the signal significantly different from the other EIP sferic components; this finding is not consistent with the smoothness that an EIP sferic should exhibit [15]. The time and width of the relatively high-frequency signal in Fig. 5(g) are consistent with those of the VHF radiation signal near 3291 μs in Fig. 1 to a certain extent, but there seems to be some difference. Combined with the location information obtained by the INTF, we find that the continuous FPB and FNB and the coincident VHF radiation signals are consistent with the development characteristics and signal characteristics of a typical NBE [19], [30]. Then, the "platform" on the EIP sferic in Fig. 5(e) should be the consequence of the LF component generated by the NBE-like event offsetting the polarity of the smooth EIP waveform.

The decomposition and reconstruction of the EIP sferic by EEMD cannot directly obtain such an NBE-like event, which is consistent with various observations. Therefore, how to construct such an NBE-like event is crucial to analyzing the physical mechanism responsible for EIP events. However, EEMD undoubtedly provides an effective means to obtain the local features of EIP sferics. Starting from these local features and using DBM_EEMD to accurately decompose and reconstruct the signal seems to be an innovative approach to obtain an NBE-like event that is consistent with various observations.

IV. Reconstruction of the EIP Sferic

Starting from the local characteristics of the IMF components obtained by EEMD, we construct the NBE-like sferic. If the constructed sferic signal and VHF signal have the same characteristics in the time domain and the same peak time, then the event associated with the constructed sferic is consistent with typical breakdown processes/streamer activity. The sferic variation characteristics of the constructed signal conform to the polarity characteristics of the electric field change produced by the FPB and FNB obtained by the INTF. The other characteristics of the signal are consistent with the signal of a typical lightning discharge. Moreover, the filtered EIP sferic acquired after removing the constructed NBE-like sferic from the original sferic should be smoother if the EIP is produced solely by relativistic discharges. In addition, since the VHF signal and the EIP sferic have different characteristics in the time domain, the generation mechanism responsible for the EIP would certainly not be typical breakdown processes/streamer activity.

Fig. 6 shows a flowchart of the 11 steps detailing how to use DBM_EEMD to decompose the sferic of the NBE-like event from the original EIP sferic. These steps can be summarized as follows: decomposition of the local sferic to obtain the

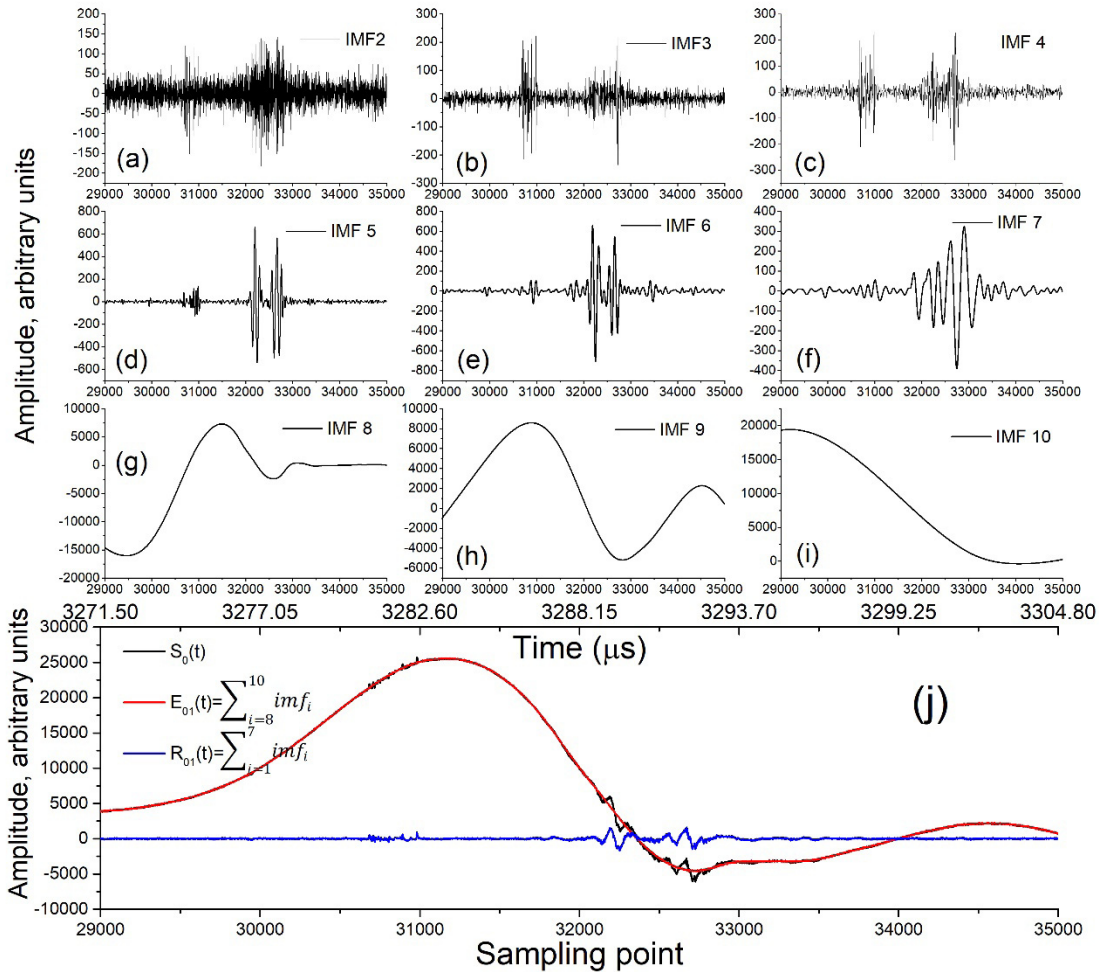

Fig. 7. In step 1, $S_O(t)$ is decomposed by EEMD and then reconstructed. (a)–(i) IMF components obtained by decomposition. (j) Reconstruction results for IMFs in different frequency bands compared with the original sferic. The lower horizontal axis coordinates of all the subgraphs denote the sampling points. To facilitate a comparison, the time is added to the upper horizontal axis of (j), and the unit is μs (since IMFs 1–4 are high-frequency components, the signal characteristics are similar, and the amplitudes are very small, so we will not show these IMFs later; instead, we will show only IMFs 5–10 in each step).

characteristics of the IMFs in every step (D: decomposition); amplification of the local signal characteristics in steps 2 and 6 (A: amplification); and smoothing, filtering and noise reduction of the signals in steps 3–5 and steps 7–11 (F: filtering). All these steps are based on the decomposition of the sferic by DBM_EEMD. As mentioned above, the HHT has been widely developed and applied in many fields for its excellent performance in signal analysis, filtering, and noise reduction [33]. In this article, the IMF components were amplified by local features and then smoothed and filtered to construct two independent signals that are consistent with observations. This approach is an innovation of the application of the EEMD method. According to the operation steps, this method is summarized as DAF. According to observations, the DAF method can be employed to construct two signals that cannot be directly observed. We compare this technique to a kind of data acquisition facility or data analysis facility.

From the decomposition and reconstruction of the EIP sferic in Figs. 3 and 4, a local signal consistent with various observations cannot be obtained directly. Therefore, we change the focus of the analysis to a local sferic and adjust the range of the target signal according to the needs in different steps.

A. FNB Part

First, we decompose the sferic in the time range of 3271.5–3304.8 μs (corresponding to 6000 sampling points) to obtain the IMFs and reconstruction results shown in Fig. 7. The basis of waveform reconstruction is similar to that in Fig. 5, that is, the spectral characteristics of each IMF component. According to the morphology of the IMF components in Fig. 7, the three IMFs numbered 8–10 with relatively low frequencies contain the main information of the EIP sferic, especially IMF 9 and IMF 10, which have very smooth waveforms. In contrast, there are some weak fluctuations in the IMF 8 waveform, reducing the smoothness of the overall waveform. Especially near sampling point 32 500 (corresponding time of 3291 μs), IMF 8 reaches a minimum value, which is consistent with the peak time of the VHF radiation signal and the transition time between the FPB and FNB [shown in Fig. 1(a)]; compared with that on the left, the sferic on the right side of sampling point 32 500 has more information (stronger volatility), while the sferic on the left side is smoother. Therefore, we reconstruct the waveforms of IMFs 8–10 with lower frequencies to obtain E_{O1} and analyze the sferic corresponding to FNB in the time domain.

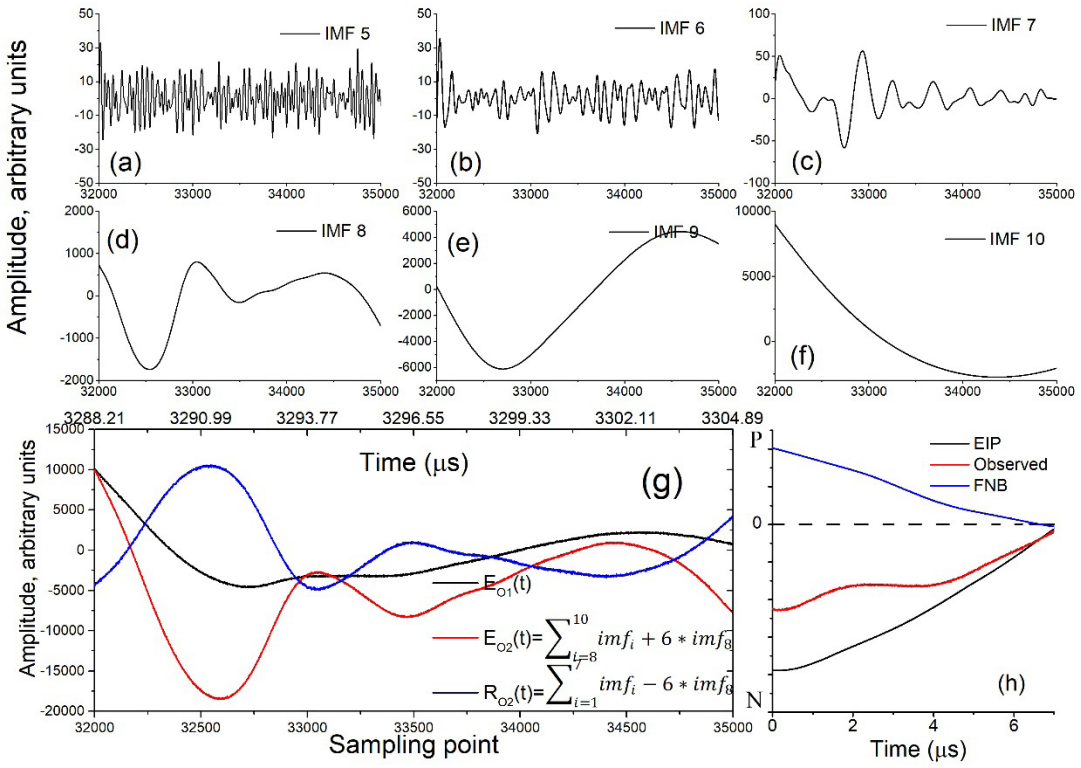

Fig. 8. In step 2, $E_{O1}(t)$ is decomposed by EEMD and then reconstructed. (a)–(f) IMF components. (g) Reconstruction results of the IMFs in different frequency bands and the comparison with the original signal, where the amplitude of IMF 8 in reconstructed signal $E_{O2}(t)$ is amplified by a factor of 6. (h) Schematic of the electric field of the upward FNB offsetting the electric field of the EIP to generate the observed electric field. P is positive, N is negative, and the dotted line is the 0 axis of the electric field value.

First, we consider the polarity of the sferic generated by the upward FNB after 3291 μs. According to the definition of the electric field change polarity in Uman *et al.* [37] and the research on fast breakdowns [19], [30], the electric field generated by the upward FNB should have the trend manifesting as the blue line in Fig. 8(h). The FA-observed sferic is the superposition of the sferic generated by the FNB and the sferic generated by the EIP process [as shown in Fig. 8(h)]. Therefore, constructing a waveform that has a larger amplitude than the actual measured sferic waveform [similar to the black line and red line in Fig. 8(h)] while ensuring that the curve is smooth is a necessary step. In the second step, the signal E_{O1} reconstructed in the first step is used as the signal to be analyzed and is decomposed by DBM_EEMD. The obtained IMFs are shown in Fig. 8(a)–(f). After adjusting the target area to sampling points 32 000–35 000, IMF 9 and IMF 10 in Fig. 8 are still the smoothest components, whereas IMF 8 is different from IMF 8 illustrated in Fig. 7 at the corresponding positions. In addition to the minimum located near sampling point 32 500, IMF 8 has another minimum near point 33 500. This is because a change in the target area changes the local characteristics of the signal (i.e., the distribution of the maximum and minimum points of the time-series signal), which changes the spline interpolation curve and thus the decomposition result. However, it should be noted that regardless of how the target area is changed, the amplitude of the decomposed IMF component is smaller than that of the original signal. This feature of the EEMD algorithm inspired us to change the maximum and minimum amplitudes of the signal through amplification (A) and then utilize the filtering (F) ability of EEMD to obtain a smooth signal with a larger amplitude.

After a comparison with the VHF radiation signal and FNB positioning information and after implementing decomposition, we amplified IMF 8 in Fig. 8(e) by a factor of 6 as an auxiliary signal and obtained $E_{O2}(t)$ [red line in Fig. 8(g)] as the signal to be decomposed; the target area was adjusted to sampling points 32 000–37 000. This sferic with a larger range was selected to smooth $E_{O2}(t)$ with the help of the EIP sferic signal trend itself. The decomposition results are shown in Fig. 9. Compared with the decomposition results in step 2 (Fig. 8), IMF 7 in step 3 is significantly different; that is, it contains the main fluctuation component of $E_{O2}(t)$ in the target region. The reconstructed sferic is obtained by adding IMFs 8–10, as shown by the red line in Fig. 9(g). Although the minimum value appears near 32 000 instead of 32 500, which deviates slightly from the expected curve, the resulting curve is at least smooth enough to approach the smoothness of the EIP signal.

After the sferic is smoothed by step 3, the residual signal $R_3(t)$ is shown as the black line in Fig. 10(g), and $E_{O3}(t)$ and $S(t)$ are shown as well. After the amplification in step 2 and the filtering in step 3, the deconstructed signals and the detected signal basically satisfy the analysis

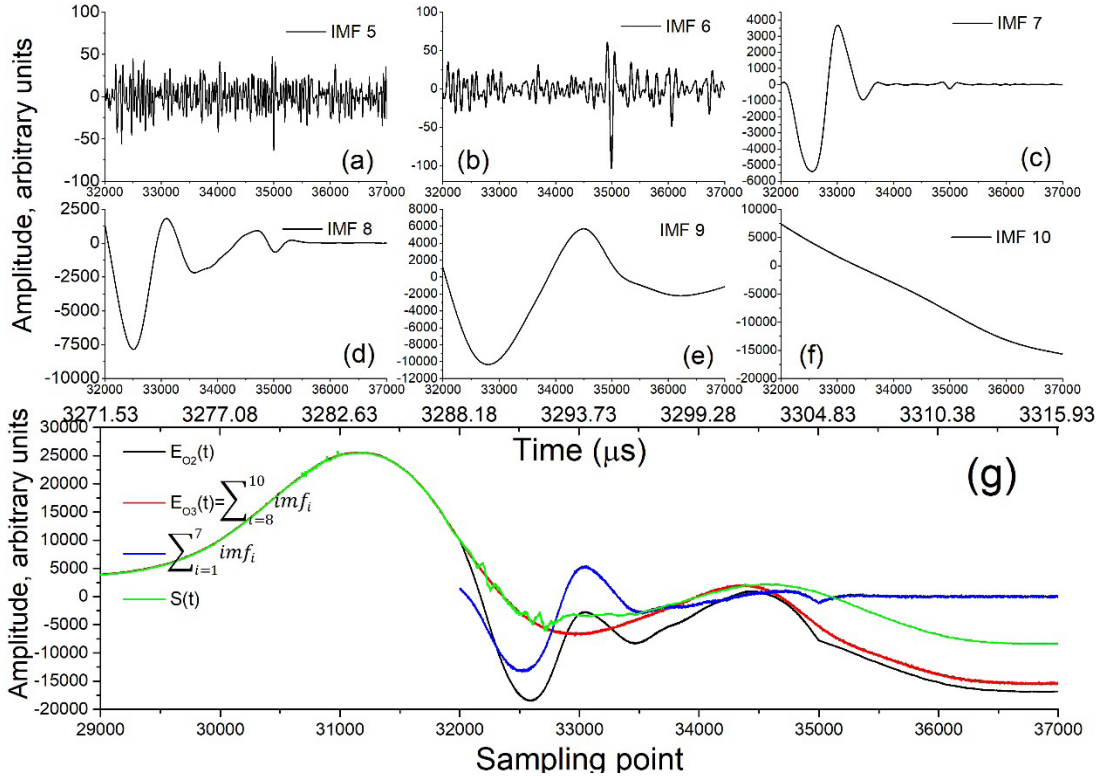

Fig. 9. In step 3, $E_{O2}(t)$ is decomposed by EEMD and then reconstructed, and the target region is adjusted to sampling points 32 000–37 000. (a)–(f) IMFs obtained by decomposition. (g) Reconstruction results of the IMF components in different frequency bands and a comparison with the original signal.

requirements in Fig. 8(h). However, after expanding the target area, we find a "step" jump in the tail of $R_3(t)$, which is not in accordance with the observations; that is, the signal containing this jump should be compensated to match the EIP sferic. We adjust the target region to sampling points 34 000–37 000, extract the range from the time when the signal starts to jump until the signal becomes flat in $R_3(t)$, and take the result as $R_{O3}(t)$ and then decompose it with EEMD. As seen from Fig. 10, the signal with weak noise is decomposed into IMFs 1–7, and the component with the signal jump is decomposed into IMFs 8–10. Therefore, we compensate for the sum of IMFs 8–10 for the EIP sferic and obtain $E_4(t)$; then, we obtain $R_4(t) = S(t) - E_4(t)$.

The compensated $E_4(t)$ is shown in Fig. 11, and the target area is adjusted to sampling points 29 000–37 000. Because $E_i(t) = S(t) - R_i(t)$ is calculated many times in the signal decomposition and reconstruction of the previous steps, the white noise phase in different steps will be slightly different, and the subtraction operation may locally increase the amplitude of noise; on the other hand, when the target area is connected with the left and right segments of the signal, the presence of noise may also cause an increase in noise. As seen from the decomposition results of $E_{O4}(t)$ in Fig. 11, the noise components in IMFs 5–7 are significantly stronger than those in the corresponding IMFs in the first two steps. These noise components need to be filtered out to ensure the smoothness of the EIP sferic.

In this way, two sferics are obtained through decomposition (D), amplification (A), and filtering (F) in the above steps: $E_5(t)$ [the black line in Fig. 11(g)] and $R_5(t)$ [the red line in Fig. 11(g)]. In the time domain of the FNB, the reconstructed sferic waveforms are basically consistent with the observations, which makes the EIP sferic smoother, and the sferic of the FNB basically matches the VHF signals and positioning results of the upward FNB in the time domain. Next, we construct the sferic waveform generated by the downward FPB.

B. FPB Part

As shown in Fig. 1(a), the positioning result obtained by the INTF shows that the downward FPB starts at 3284 μs and transitions to upward FNB at 3291 μs. Similarly, we consider the polarity and morphology of the sferic generated by the downward FPB after 3284 μs. Similar to the analysis of the upward FNB in step 2, according to the definition of the electric field polarity in Uman *et al.* [37] and the research on fast breakdowns [19], [30], the sferic generated by the downward FPB should be similar to the changing trend manifesting as the blue line in Fig. 12(h), although the sferic measured by the FA is the superposition of the sferics generated by the downward FPB and the EIP [as shown in Fig. 12(h)]. It should be noted that although the start time of the downward FPB obtained by the INTF is 3284 μs, this does not mean that the electric field generated by the FPB can be detected by the FA from 3284 μs. This is because the electrostatic field is the time integral of the current (charge), and the electrostatic field needs a certain amount of time and accumulation to show significant changes. On the other hand, the attenuation of the electrostatic field itself with distance is

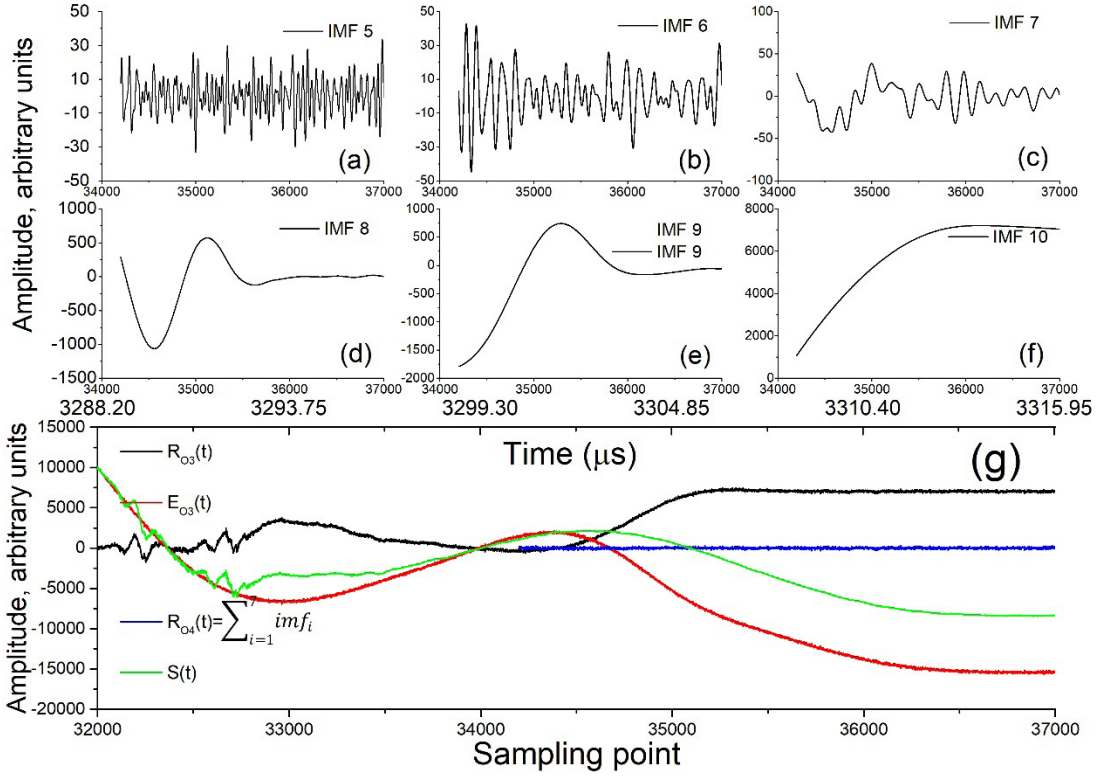

Fig. 10. In step 4, $R_{O3}(t)$ was decomposed by EEMD and then reconstructed, and the target area was adjusted to sampling points 34 000–37 000. The purpose of this step is to decompose the step "jump" in $R_{O3}(t)$ and compensate it into the EIP sferic. (a)–(f) Decomposed IMFs. (g) Reconstruction results of the IMF components in different frequency bands and the comparison with the original signal.

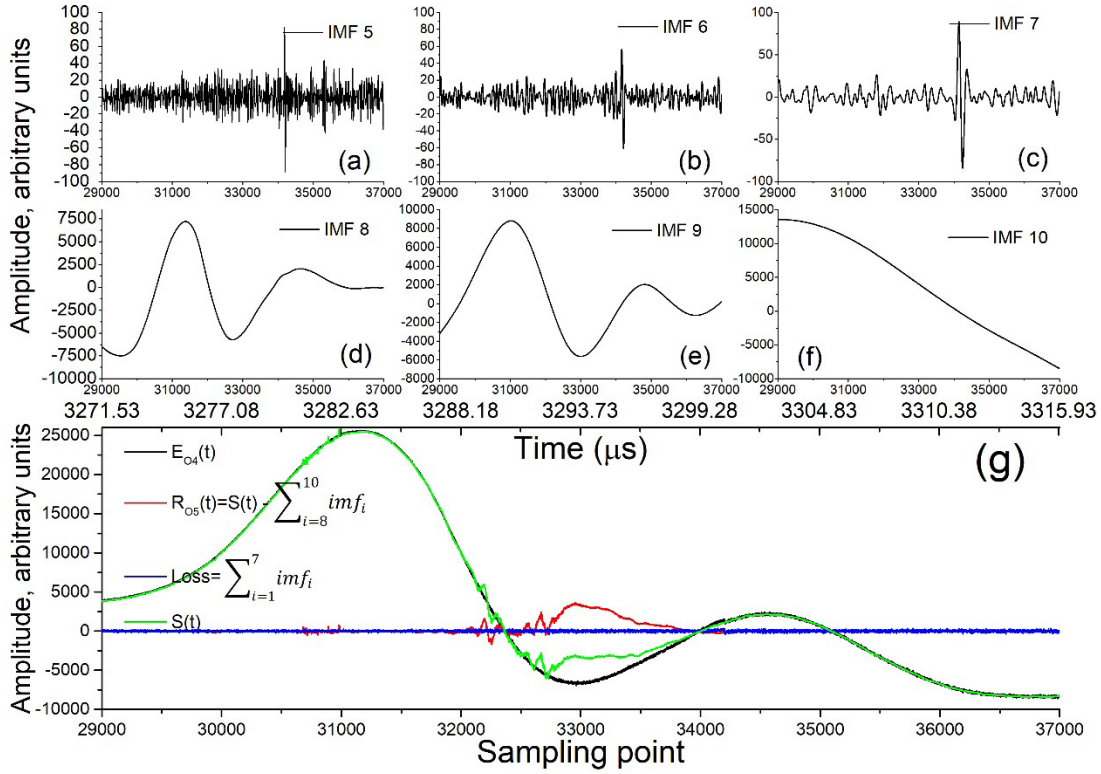

Fig. 11. In step 5, $E_{O4}(t)$ was decomposed by EEMD and then reconstructed, and the target region was adjusted to sampling points 29 000–37 000. The purpose of this step is to remove the increased white noise in $E_{O4}(t)$ due to $E_i(t) = S(t) - R_i(t)$. (a)–(f) Decomposed IMFs. (g) Reconstruction results of the IMF components in different frequency bands and the comparison with the original sferic.

very serious; consequently, the FPB information that the INTF can obtain is acquired earlier than the information obtained by the FA. Combined with the analysis of Fig. 12(h) and steps 2–4, it seems that the EIP sferic in Fig. 12(h) can be

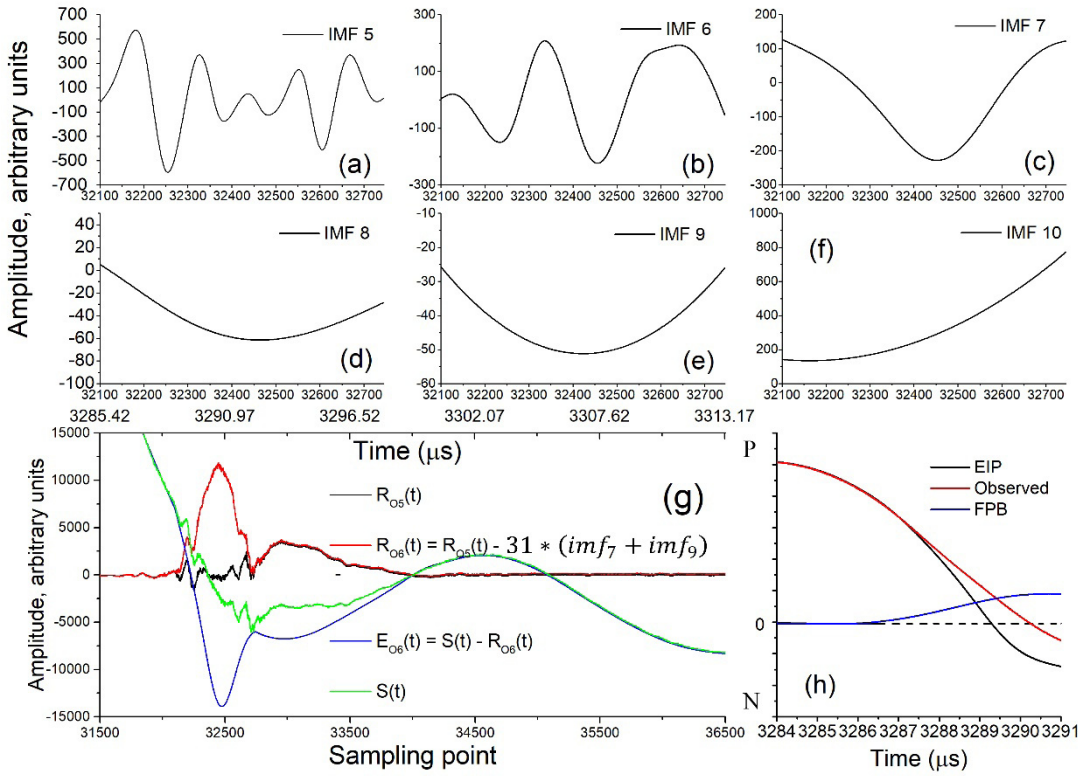

Fig. 12. In step 6, $R_{O5}(t)$ is decomposed by EEMD and then reconstructed. (a)–(f) IMF components. (g) Reconstruction results of the IMFs in different frequency bands and the comparison with the original signal, where the amplitudes of IMF 7 and IMF 9 in the reconstructed signal $R_{O6}(t)$ are amplified by a factor of 30. (h) Schematic of the electric field of the downward FPB offsetting the electric field of the EIP to generate the observed electric field. P is positive, N is negative, and the dotted line is the 0 axis of the electric field value.

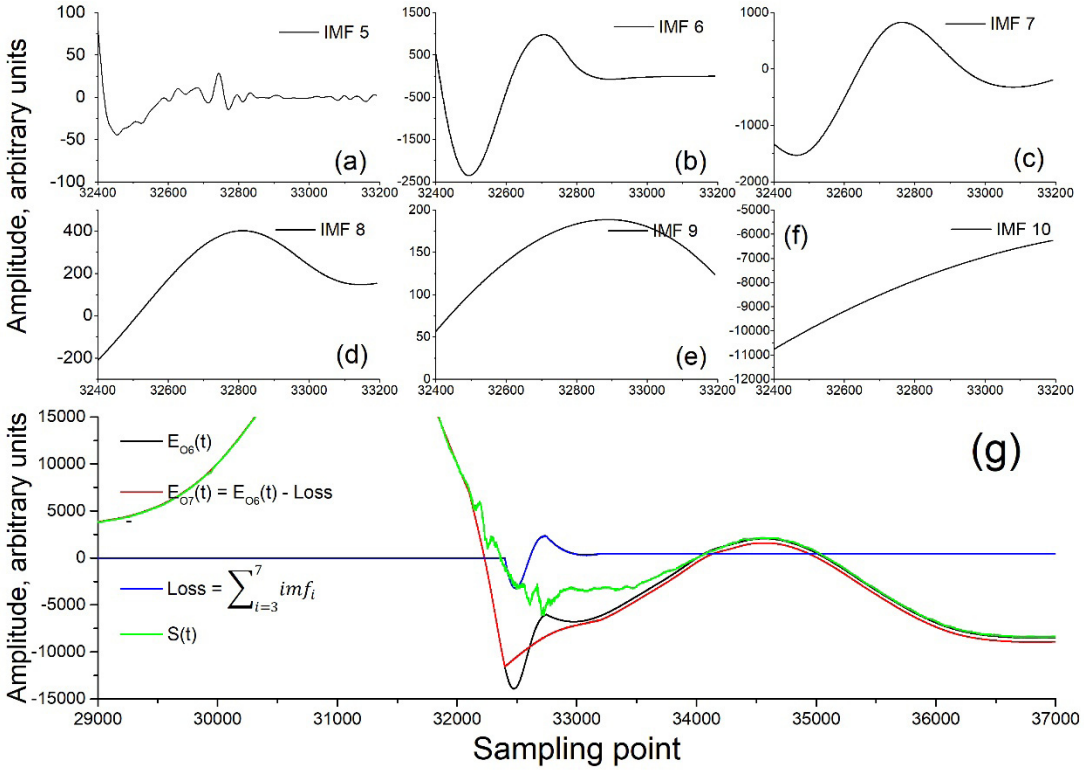

Fig. 13. In step 7, $E_{O6}(t)$ is decomposed by EEMD and then reconstructed. (a)–(f) IMFs obtained by decomposition. (g) Reconstruction results of the IMF components in different frequency bands and the comparison with the original signal.

constructed from either $E_5(t)$ or $R_5(t)$. However, considering that the amplitude of $E_5(t)$ corresponding to the time domain of the downward FPB is excessively large, it is difficult to control the amplification factor. The amplitude of the sferic

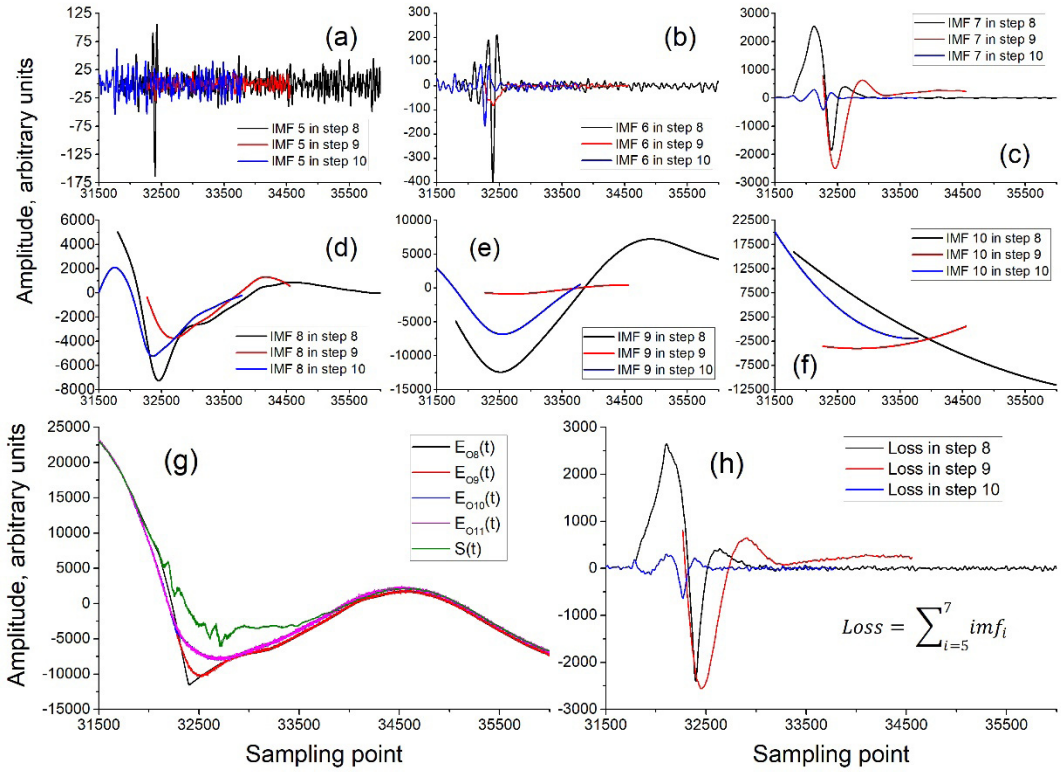

Fig. 14. In steps 8–10, $E_{Oi}(t)$ $(i = 7, 8, 9)$ is decomposed by EEMD and then reconstructed. (a)–(f) IMFs obtained by decomposition. (g) Reconstruction results of the IMF components in different frequency bands and the comparison with the original signal. (h) To ensure the smoothness of the EIP sferic in different steps, these components are removed from $E_{Oi}(t)(i = 7, 8, 9)$.

in $R_5(t)$ corresponding to the downward FPB time domain is much smaller than that in $E_5(t)$, so it is easy to adjust the amplification factor. Therefore, we start with $R_5(t)$ to analyze the downward FPB.

The results of the decomposition of $R_{O5}(t)$ by EEMD and the reconstruction of the signal in step 6 are shown in Fig. 12. The target region was adjusted to sampling points 32 100–32 750. This target region was selected to decompose components with even ends such as IMF 7 and IMF 9 in Fig. 12(c) and (e). The advantage of flattening both ends of these IMF components is that no matter how many times the signal is increased, the connection at the right end of the signal will not be affected, thus avoiding the appearance of a stepped waveform such as $R_{O3}(t)$, which requires one step to eliminate. There is a minimum value near point 32 500 (3291 μs) in the decomposed IMF 7, IMF 8, and IMF 9, which is consistent with the peak time of the VHF radiation waveform and the transition time between the FPB and FNB. This feature can always be obtained when $R_{O5}(t)$ is decomposed by changing the target area, which is very important. To obtain the electric field curves of the EIP and downward FPB analyzed in Fig. 12(h), we reverse-amplify IMF 7 and IMF 9 by a factor of 30 to obtain $R_{O6}(t)$ and $E_{O6}(t)$ (they are characterized by equal values at both ends of the target region). Note that $R_{O6}(t) + E_{O6}(t) = S_{O6}(t)$ is still satisfied. The obtained $E_{O6}(t)$ is not smooth, so we need to smooth $E_{O6}(t)$ according to the principle of DAF.

Fig. 13 illustrates the decomposition of $E_{O6}(t)$ in step 7. After the initial deconstruction of the electric field of the FNB, the EIP sferic is very smooth except for the pulse-shaped bulge (the peak at 32 500) reconstructed in step 6. $E_{O6}(t)$ cannot be smoothed by the EIP sferic trend characteristics (as in step 3). This is because the frequency difference of the pulse constructed in step 6 is too high compared with the other parts of the EIP sferic. If the pulse is decomposed directly, the same waveform as $31 \times (\text{imf7} + \text{imf9})$ in Fig. 12 will always be obtained, so it is impossible to construct a sferic generated by a downward FPB. Therefore, we tried to adjust the target area to construct the FPB sferic gradually. Therefore, the selection of the target area (sampling points 32 400–33 200) in step 7 removes the convex head in $E_{O6}(t)$ and controls the minimum range of the EIP sferic near point 32 500 obtained in the preceding step, which also controls the amplitude of the electric field related to the NBE-like event.

As in step 7, we continue to repeat the filtering operations for three steps. The decomposition results of $E_{Oi}(t)$ $(i = 7, 8, 9)$ after each step in Fig. 14 demonstrate that the unsmooth component in $E_{Oi}(t)$ gradually decreases (IMFs 5–7), while the smoothness is gradually enhanced. After removing the unsmooth component from $E_{Oi}(t)$ in each step, we finally obtained a sufficiently smooth EIP sferic $[E_{10}(t)]$, which is consistent with the observations.

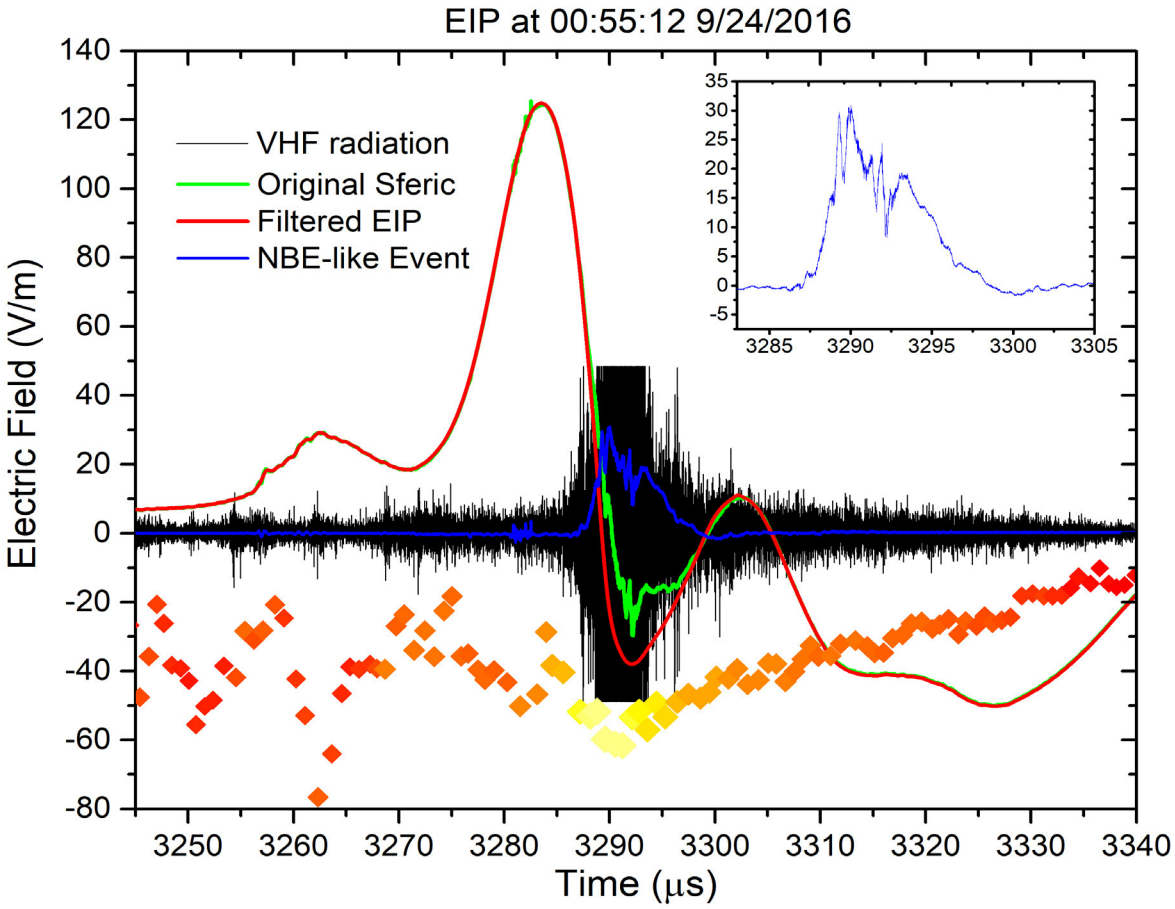

Fig. 15. EEMD [22] is utilized to extract the NBE-like perturbation from the EIP sferic in a manner that illustrates the true amplitude of the initial part of the sferic. The remaining (red) waveform is that of the relativistic discharge(s).

C. Filtered EIP and Constructed NBE-Like Sferic

As in step 5, noise may be retained or introduced into the obtained EIP sferic after multiple steps of decomposition, reconstruction, and connection among the left, objective, and right segments of the sferic. Therefore, after filtering the complete sferic $E_{11}(t)$ in step 11 (similar to step 5), we finally separated a pure EIP sferic and constructed a sferic of an NBE-like event. The final decomposition results are shown in Fig. 15. Here, we return to the selection of the amplification factor in step 2 and step 6. The amplification factors (30 in the reconstruction of the downward FPB electric field and 6 in the reconstruction of the upward FNB electric field) are the results of appropriate adjustments after the establishment of the whole DAF method. These two factors are selected to ensure that the sferic of the final constructed NBE-like event matches the observations. On the other hand, the selection of these two parameters determines the electric field amplitude of the NBE-like event. Changing these two parameters will cause the NBE-like event to be inconsistent with the observations in the time domain and affect the smoothness of the EIP sferic.

Through the above 11 steps, EEMD is used to decompose (D) the signal repeatedly, amplify (A) the local signal features, and smooth and filter (F) the signal; finally, the observed EIP sferic is decomposed into two components, namely, a smoother EIP sferic and an NBE-like sferic, which is consistent with various observational facts. The sferic characteristics of the NBE-like event and VHF signal have the same change trend in the time domain and the same peak time; moreover, the sferic change characteristics of the NBE-like event are consistent with the downward FPB and the upward FNB obtained by the INTF. In addition, the peak current moment (−26.1 kA·km) and charge-moment change (0.62 C·km) of the NBE-like event are consistent with other NBE observations [19], [22], [30]. The resulting filtered EIP sferic gives a slightly higher peak current moment (−298.3 kA·km) and smaller charge-moment change (13.1 C·km) than the unfiltered values reported by Tilles *et al.* [18].

The above signal analysis, decomposition, and reconstruction fully confirm that part of the signal superimposed on the FA-observed EIP sferic originated from an NBE-like event and that the strong VHF radiation that does not match the peak value of the EIP sferic was generated by this NBE-like event, which indicates that the EIP itself did not radiate a VHF radio signal. Ultimately, the analysis, decomposition, and reconstruction of the correlated signals by the EEMD-based DAF method proposed in this article are combined with the analysis of Tilles *et al.* [18] to support the idea that the large-amplitude EIP sferic was generated by the relativistic discharge responsible for an accompanying TGF rather than by streamer or leader activity.

V. Discussion

EMD is an empirical signal analysis method that has not been proven by strict mathematics, hence the meaning of "empirical" in EMD [32]. That the EMD method lacks a strict mathematical proof appears to be a defect, but this shortcoming has not restricted the continuous improvement and wide application of EMD. For a signal, changing the signal length (target area) decomposed by EEMD will change the decomposition result, but it will not change the frequency band range of each IMF component. The EEMD method is based on the interpolation of the local maximum and minimum of the signal (as shown in Fig. 3). Therefore, changing the extrema of the signal can change the decomposition result of the signal. Furthermore, a smooth signal can be obtained between the maximum and minimum by using the signal smoothing ability of EEMD (sifting IMFs). This is the core idea of the EEMD-based DAF method proposed in this article. The step-by-step application of the DAF technique is based on the comprehensive analysis of various observations to fully understand and deconstruct the local characteristics of signals in detail. In this article, changing the target area of the decomposed signal and amplifying specific IMF components are implemented to change the local characteristics of the signal, which is an innovative application of the EEMD method, although such innovation is also based on experience.

In addition, from an empirical perspective, we believe that, based on EEMD and guided by the DAF method, two sferics can be deconstructed following completely different steps from those described in this article. However, the two sferics must satisfy the following observations: the sferics of an NBE-like event and a VHF signal should have the same characteristics in the time domain and the same peak time. The sferic of NBE-like event is consistent with the downward FPB then upward FNB observed by the INTF. The other quantitative characteristics of such sferics are consistent with the typical NBE lightning discharge signals. In addition, after removing the sferics of NBE-like events from the original EIP sferic, the obtained EIP sferic should be smoother if caused by a relativistic discharge. Under the constraints of these observations, the morphologies of the sferics of the NBE-like event and the EIP event are unique. Therefore, although the EEMD-based DAF method is also based on empirical analysis in deconstructing signals, it is a very effective method from the perspective of analyzing the specific physical lightning discharge process. Based on the analysis, decomposition and reconstruction of the correlated signals based on the method proposed in this article, together with the analysis of Tilles *et al.* [18], we determined that the EIP was not generated by breakdown processes/streamer activity; instead, its generation mechanism is a relativistic feedback discharge (RFD). The above observations and analysis provide a clear indication that the smooth component of the EIP sferic was produced separately from that produced by the VHF-radiating fast breakdown processes. The smooth component was presumably produced by an RFD, which would not have radiated strongly at VHF [38], whereas VHF signals are generally associated with streamer activity [19]–[21].

TABLE I
Abbreviations in This Article

Abbreviation	The original meaning of abbreviation
DAF	DAF method for signal construction is proposed that repeatedly decomposes (D) the signal, amplifies (A) the local signal characteristics, and then filters (F) the signal.
DBM	double-sided bidirectional mirror extension
EIP	energetic in-cloud pulse
EMD	empirical mode decomposition
EEMD	ensemble empirical mode decomposition
FA	fast antenna
FFT	fast Fourier transform
FNB	fast negative breakdowns
FPB	fast positive breakdowns
HHT	Hilbert-Huang transform
IMFs	intrinsic mode functions
INTF	interferometer
KSC	Kennedy Space Center
LF	low-frequency
LFEDAs	low-frequency E-field detection arrays
LMA	Lightning Mapping Array
NBE	narrow bipolar event
NLDN	National Lightning Detection Network
NMT	New Mexico Tech
RFD	relativistic feedback discharge
TGF	terrestrial gamma-ray flash
VHF	very high-frequency
VLF	very low-frequency

The observation of lightning electromagnetic signals is a very complex problem. Breakdown processes/streamer activity can produce VHF radiation, and continuous breakdown processes/streamer activity can also produce electric field changes in the LF/VLF frequency band. Generally, lightning signals of different frequency bands evolve in a similar manner in the time domain. However, EIP signals are caused by RFDs, which would not produce VHF/UHF radiation but would produce strong LF/VLF signals. As in this article, EIP and NBE-like events together cause electric field changes at observation stations; the observed signal appears visually, but this does not necessarily mean that it reflects reality. Differentiating between the two types of superimposed signals, each produced by different physical mechanisms, is demonstrated in this article.

Through the EMD algorithm and its improved form already have unique advantages in lightning electromagnetic field signal analysis and lightning location [23], [31], we show an innovative application of the EMD algorithm to obtain new and important information in the analysis of thunderstorm relativistic discharges. In fact, EMD can also play an important role in the rapid detection of special signals such

as EIPs. From the present results and the observations of other studies, EIPs have larger waveform amplitude and wider time scale, corresponding to lower spectral characteristics, and occur in the initial stage of lightning. Based on the above characteristics, we assume that if we can obtain the electric field waveforms of some typical EIPs, we can use HHT (EEMD + Hilbert transform) to obtain the time–frequency distribution characteristics of these EIPs. According to these spectrum characteristics, we can easily detect EIPs from the time–frequency spectrum of electric field waveforms at the initial stage of lightning (within the first ten milliseconds of IC flashes [39]. We expect the EMD algorithm to be utilized and applied more extensively in future lightning research.

Appendix

Many abbreviations are used in this article. For the convenience of readers, the abbreviations in this article are listed in Table I.

Acknowledgment

The authors would like to thank the editors and the anonymous reviewers for their constructive comments and suggestions, which greatly helped them to improve the technical quality and presentation of this article.

References

[1] G. J. Fishman *et al.*, "Discovery of intense gamma-ray flashes of atmospheric origin," *Science*, vol. 264, no. 5163, pp. 1313–1316, May 1994, doi: 10.1126/science.264.5163.1313.

[2] O. J. Roberts *et al.*, "The first Fermi -GBM terrestrial gamma ray flash catalog," *J. Geophys. Res., Space Phys.*, vol. 123, no. 5, pp. 4381–4401, May 2018, doi: 10.1029/2017JA024837.

[3] B. G. Mailyan *et al.*, "Gamma-ray and radio-frequency radiation from thunderstorms observed from space and ground," *Sci. Rep.*, vol. 10, no. 1, p. 7286, Dec. 2020, doi: 10.1038/s41598-020-63437-2.

[4] M. A. Stanley *et al.*, "A link between terrestrial gamma-ray flashes and intracloud lightning discharges," *Geophys. Res. Lett.*, vol. 33, no. 6, 2006, Art. no. L06803, doi: 10.1029/2005gl025537.

[5] X.-M. Shao, T. Hamlin, and D. M. Smith, "A closer examination of terrestrial gamma-ray flash-related lightning processes," *J. Geophys. Res., Space Phys.*, vol. 115, no. A6 Jun. 2010, Art. no. A00E30, doi: 10.1029/2009ja014835.

[6] G. Lu, S. A. Cummer, J. Li, F. Han, D. M. Smith, and B. W. Grefenstette, "Characteristics of broadband lightning emissions associated with terrestrial gamma ray flashes," *J. Geophys. Res., Space Phys.*, vol. 116, no. A3, Mar. 2011, Art. no. A03316, doi: 10.1029/2010ja016141.

[7] S. A. Cummer, F. Lyu, M. S. Briggs, G. Fitzpatrick, O. J. Roberts, and J. R. Dwyer, "Lightning leader altitude progression in terrestrial gamma-ray flashes," *Geophys. Res. Lett.*, vol. 42, no. 18, pp. 7792–7798, Sep. 2015, doi: 10.1002/2015gl065228.

[8] G. Lu *et al.*, "Lightning mapping observation of a terrestrial gamma-ray flash," *Geophys. Res. Lett.*, vol. 37, no. 11, Jun. 2010, Art. no. L11806, doi: 10.1029/2010gl043494.

[9] F. Lyu *et al.*, "Very high frequency radio emissions associated with the production of terrestrial gamma-ray flashes," *Geophys. Res. Lett.*, vol. 45, no. 4, pp. 2097–2105, Feb. 2018, doi: 10.1002/2018gl077102.

[10] B. G. Mailyan *et al.*, "Characteristics of radio emissions associated with terrestrial gamma-ray flashes," *J. Geophys. Res., Space Phys.*, vol. 123, no. 7, pp. 5933–5948, Jul. 2018, doi: 10.1029/2018ja025450.

[11] E. R. Williams, "The tripole structure of thunderstorms," *J. Geophys. Res., Atmos.*, vol. 94, no. D11, pp. 13151–13167, 1989, doi: 10.1029/jd094id11p13151.

[12] S. A. Cummer *et al.*, "The lightning-TGF relationship on microsecond timescales," *Geophys. Res. Lett.*, vol. 38, no. 14, Jul. 2011, Art. no. 14810, doi: 10.1029/2011gl048099.

[13] Y. Pu *et al.*, "Low frequency radio pulses produced by terrestrial gamma-ray flashes," *Geophys. Res. Lett.*, vol. 46, no. 12, pp. 6990–6997, Jun. 2019, doi: 10.1029/2019gl082743.

[14] S. A. Cummer *et al.*, "The source altitude, electric current, and intrinsic brightness of terrestrial gamma ray flashes," *Geophys. Res. Lett.*, vol. 41, no. 23, pp. 8586–8593, Dec. 2014, doi: 10.1002/2014gl062196.

[15] F. Lyu, S. A. Cummer, and L. McTague, "Insights into high peak current in-cloud lightning events during thunderstorms," *Geophys. Res. Lett.*, vol. 42, no. 16, pp. 6836–6843, Aug. 2015, doi: 10.1002/2015gl065047.

[16] F. Lyu *et al.*, "Ground detection of terrestrial gamma ray flashes from distant radio signals," *Geophys. Res. Lett.*, vol. 43, no. 16, pp. 8728–8734, Aug. 2016, doi: 10.1002/2016gl070154.

[17] S. A. Cummer *et al.*, "The connection between terrestrial gamma-ray flashes and energetic in-cloud lightning pulses," in *Proc. AGU Fall Meeting*, New Orleans, LA, USA, Nov. 2017, pp. AE33B–2547.

[18] J. N. Tilles *et al.*, "Radio interferometer observations of an energetic in-cloud pulse reveal large currents generated by relativistic discharges," *J. Geophys. Res., Atmos.*, vol. 125, no. 20, Art. no. e2020JD032603, Oct. 2020, doi: 10.1029/2020JD032603.

[19] W. Rison *et al.*, "Observations of narrow bipolar events reveal how lightning is initiated in thunderstorms," *Nature Commun.*, vol. 7, no. 1, Apr. 2016, Art. no. 10721, doi: 10.1038/ncomms10721.

[20] F. Shi, N. Liu, and H. K. Rassoul, "Properties of relatively long streamers initiated from an isolated hydrometeor," *J. Geophys. Res., Atmos.*, vol. 121, no. 12, pp. 7284–7295, Jun. 2016, doi: 10.1002/2015jd024580.

[21] F. Shi, N. Liu, J. R. Dwyer, and K. M. A. Ihaddadene, "VHF and UHF electromagnetic radiation produced by streamers in lightning," *Geophys. Res. Lett.*, vol. 46, no. 1, pp. 443–451, Jan. 2019, doi: 10.1029/2018gl080309.

[22] N. Liu *et al.*, "Understanding the radio spectrum of thunderstorm narrow bipolar events," *J. Geophys. Res., Atmos.*, vol. 124, nos. 17–18, pp. 10134–10153, Sep. 2019, doi: 10.1029/2019jd030439.

[23] X. Fan *et al.*, "Application of ensemble empirical mode decomposition in low-frequency lightning electric field signal analysis and lightning location," *IEEE Trans. Geosci. Remote Sens.*, vol. 59, no. 1, pp. 86–100, Jan. 2021, doi: 10.1109/TGRS.2020.2991724.

[24] W. Rison, R. J. Thomas, P. R. Krehbiel, T. Hamlin, and J. Harlin, "A GPS-based three-dimensional lightning mapping system: Initial observations in central new mexico," *Geophys. Res. Lett.*, vol. 26, no. 23, pp. 3573–3576, Dec. 1999, doi: 10.1029/1999gl010856.

[25] R. J. Thomas, "Accuracy of the lightning mapping array," *J. Geophys. Res.*, vol. 109, no. D14, 2004, Art. no. D14207, doi: 10.1029/2004jd004549.

[26] M. G. Stock *et al.*, "Continuous broadband digital interferometry of lightning using a generalized cross-correlation algorithm," *J. Geophys. Res., Atmos.*, vol. 119, no. 6, pp. 3134–3165, Mar. 2014, doi: 10.1002/2013jd020217.

[27] X. M. Shao, P. R. Krehbiel, N. J. Thomas, and W. Rison, "Radio interferometric observations of cloud-to-ground lightning phenomena in Florida," *J. Geophys. Res., Atmos.*, vol. 100, no. D2, pp. 2749–2783, Feb. 1995, doi: 10.1029/94jd01943.

[28] X. M. Shao and P. R. Krehbiel, "The spatial and temporal development of intracloud lightning," *J. Geophys. Res., Atmos.*, vol. 101, no. D21, pp. 26641–26668, Nov. 1996, doi: 10.1029/96jd01803.

[29] O. A. van der Velde and J. Montanyà, "Asymmetries in bidirectional leader development of lightning flashes," *J. Geophys. Res., Atmos.*, vol. 118, no. 24, Dec. 2013, Art. no. 13504, doi: 10.1002/2013jd020257.

[30] J. N. Tilles *et al.*, "Fast negative breakdown in thunderstorms," *Nature Commun.*, vol. 10, no. 1, p. 1648, Dec. 2019, doi: 10.1038/s41467-019-09621-z.

[31] X. P. Fan *et al.*, "A new method of three-dimensional location for low-frequency electric field detection array," *J. Geophys. Res., Atmos.*, vol. 123, no. 16, pp. 8792–8812, Aug. 2018, doi: 10.1029/2017jd028249.

[32] N. E. Huang *et al.*, "The empirical mode decomposition and the Hilbert spectrum for nonlinear and non-stationary time series analysis," *Proc. Roy. Soc. London. Ser. A, Math., Phys. Eng. Sci.*, vol. 454, no. 1971, pp. 903–995, Mar. 1998, doi: 10.1098/rspa.1998.0193.

[33] N. E. Huang and Z. Wu, "A review on Hilbert-Huang transform: Method and its applications to geophysical studies," *Rev. Geophys.*, vol. 46, no. 2, Jun. 2008, Art. no. RG2006, doi: 10.1029/2007rg000228.

[34] X. Fan, Y. Zhang, Q. Yin, Y. Zhang, and D. Zheng, "Characteristics of a multi-stroke 'bolt from the blue' lightning-type that caused a fatal disaster," *Geomatics, Natural Hazards Risk*, vol. 10, no. 1, pp. 1425–1442, Jan. 2019, doi: 10.1080/19475705.2018.1553800.

[35] Z. Wu and N. E. Huang, "Ensemble empirical mode decomposition: A noise-assisted data analysis method," *Adv. Adapt. Data Anal.*, vol. 1, no. 1, pp. 1–41, Jan. 2009, doi: 10.1142/s1793536909000047.
[36] G. Rilling, P. Flandrin, and P. Gonlalves, "On empirical mode decomposition and its algorithms," in *Proc. IEEE-EURASIP Workshop Nonlinear Signal Image Process.*, Grado, Italy, Feb. 2003, pp. 8–11.
[37] M. A. Uman, D. K. McLain, and E. P. Krider, "The electromagnetic radiation from a finite antenna," *Amer. J. Phys.*, vol. 43, no. 1, pp. 33–38, Jan. 1975, doi: 10.1119/1.10027.
[38] J. R. Dwyer and S. A. Cummer, "Radio emissions from terrestrial gamma-ray flashes," *J. Geophys. Res., Space Phys.*, vol. 118, no. 6, pp. 3769–3790, Jun. 2013, doi: 10.1002/jgra.50188.
[39] J. W. Belz *et al.*, "Observations of the origin of downward terrestrial gamma-ray flashes," *J. Geophys. Res., Atmos.*, vol. 125, no. 23, Dec. 2020, Art. no. e2019JD031940, doi: 10.1029/2019JD031940.

Xiangpeng Fan received the B.S. degree in atmospheric sciences from Lanzhou University, Lanzhou, China, in 2008, the M.Sc. degree in atmospheric physics from the Cold and Arid Regions Environment and Engineering Research Institute, Chinese Academy of Sciences, Lanzhou, in 2011, and the Ph.D. degree in atmospheric sciences from the Chinese Academy of Sciences, Beijing, China, in 2019.

He is an Associate Professor with the State Key Laboratory of Severe Weather, Chinese Academy of Meteorological Sciences, Beijing. His research interests include lightning physics and lightning detection.

Paul R. Krehbiel received the B.Sc. and M.Sc. degrees in electrical engineering (with a physics option) from the Massachusetts Institute of Technology, Cambridge, MA, USA, in 1963 and 1966, respectively, and the Ph.D. degree in physics from the University of Manchester Institute of Science and Technology, Manchester, U.K., in 1982.

He is a Professor of Physics with the Physics Department and the Langmuir Laboratory for Atmospheric Research, New Mexico Institute of Mining and Technology, Socorro, NM, USA.

Julia N. Tilles received the B.Sc. degree from the University of Massachusetts Amherst, Amherst, MA, USA, in 2008, the M.Sc. degree from New Mexico Tech, Socorro, NM, USA, in 2015, and the Ph.D. degree from the University of New Hampshire, Durham, NH, USA, in 2020, all in physics.

She is a Post-Doctoral Researcher with the Electrical Sciences and Experiments Division, Sandia National Laboratories, Albuquerque, NM. Her research interest includes radio frequency measurements of electrical processes in thunderstorms and in the laboratory.

Mark A. Stanley received the B.S. degree in physics from Purdue University, West Lafayette, IN, USA, in 1991, the M.S. degree in astrophysics from Michigan State University, East Lansing, MI, USA, in 1992, and the Ph.D. degree in atmospheric physics from New Mexico Tech, Socorro, NM, USA, in 2000.

He is working as a Senior Research Specialist with the Langmuir Laboratory for Atmospheric Research, New Mexico Tech. His research interests include the design and operation of remote sensing systems, electrical discharge physics, software development, and large dataset analysis.

Seda Senay received the B.S. and M.S. degrees in electrical engineering from Yeditepe University, Istanbul, Turkey, in 2001 and 2005, respectively, and the Ph.D. degree in electrical engineering from the University of Pittsburgh, Pittsburgh, PA, USA, in 2011.

She is an Associate Professor of Electrical Engineering with the New Mexico Institute of Mining and Technology, Socorro, NM, USA. Her research interest is in the analysis of signals using time–frequency methods.

Harald E. Edens received the M.S. degree in physics from the University of Amsterdam, Amsterdam, The Netherlands, in 2002, and the Ph.D. degree in atmospheric physics from New Mexico Tech, Socorro, NM, USA, in 2011.

He is the Director of the Langmuir Laboratory for Atmospheric Research, a research division of New Mexico Tech. His research interests are lightning physics, lightning mapping, imaging techniques, and instrument design.

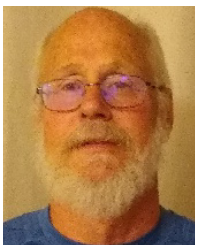

William Rison received the B.S. degree in physics from the University of Wyoming, Laramie, WY, USA, in 1973, and the Ph.D. degree in physics from the University of California at Berkeley, Berkeley, CA, USA, in 1980.

After a post-doctoral position with the Scripps Institution of Oceanography, San Diego, CA, he joined the New Mexico Institute of Mining and Technology, Socorro, NM, USA, in 1984, where he is a Research Professor of Electrical Engineering and the Langmuir Laboratory for Atmospheric Research.

Yijun Zhang received the B.Sc. degree in physics from Hebei Normal University, Shijiazhuang, China, in 1986, and the M.Sc. and Ph.D. degrees in atmospheric physics from the Cold and Arid Regions Environment and Engineering Research Institute, Chinese Academy of Sciences, Lanzhou, China, in 1989 and 1998, respectively.

He is a Professor with the Department of Atmospheric and Oceanic Sciences, Institute of Atmospheric Sciences, Fudan University, Shanghai, China. His research interests include atmospheric electricity, lightning physics, and thunderstorm electricity.